

# Clinical Metadata Guided Limited-Angle CT Image Reconstruction

Yu Shi, *Member, IEEE*, Shuyi Fan, Changsheng Fang, Shuo Han, Haodong Li, Li Zhou, Bahareh Morovati, Dayang Wang, *Senior Member, IEEE*, and Hengyong Yu, *Fellow, IEEE*

**Abstract**—Limited-angle computed tomography (LACT) offers improved temporal resolution and reduced radiation dose for cardiac imaging, but suffers from severe artifacts due to truncated projections. To address the ill-posedness of LACT reconstruction, we propose a two-stage diffusion framework guided by structured clinical metadata. In the first stage, a transformer-based diffusion model conditioned exclusively on metadata, including acquisition parameters, patient demographics, and diagnostic impressions, generates coarse anatomical priors from noise. The second stage further refines the images by integrating both the coarse prior and metadata to produce high-fidelity results. Physics-based data consistency is enforced at each sampling step in both stages using an Alternating Direction Method of Multipliers module, ensuring alignment with the measured projections. Extensive experiments on both synthetic and real cardiac CT datasets demonstrate that incorporating metadata significantly improves reconstruction fidelity, particularly under severe angular truncation. Compared to existing metadata-free baselines, our method achieves superior performance in SSIM, PSNR, nMI, and PCC. Ablation studies confirm that different types of metadata contribute complementary benefits, particularly diagnostic and demographic priors under limited-angle conditions. These findings highlight the dual role of clinical metadata in improving both reconstruction quality and efficiency, supporting their integration into future metadata-guided medical imaging frameworks.

**Index Terms**—Limited-angle CT, large language model (LLM), diffusion model, incomplete data reconstruction

## I. INTRODUCTION

CARDIAC CT is an essential modality in non-invasive cardiovascular imaging. It offers crucial structural details for the diagnosis of coronary artery disease (CAD) [1], the evaluation of myocardial perfusion [2], and preprocedural planning for structural heart interventions [3]. However, it remains challenging to achieve diagnostically reliable cardiac CT images due to rapid heart movement, imposing stringent demands on temporal resolution. To mitigate cardiac motion artifacts, ECG gating techniques are commonly employed [4], [5], yet they inherently prolong acquisition time, increase

radiation exposure, and remain vulnerable to motion artifacts, especially in patients with irregular heart rates [6]. Moreover, the reliance on full angular scan in CT reconstruction further limits temporal resolution in dynamic cardiac imaging.

Limited-angle computed tomography (LACT) has emerged as a promising solution to these challenges in cardiac CT [7]. By acquiring projections over a reduced angular range, LACT improves temporal resolution and reduces radiation dose. However, the resulting angular truncation renders the reconstruction process highly ill-posed, often introducing pronounced artifacts such as streaks, structural blurring, and intensity bias [8], especially near anatomical boundaries.

Classical analytical methods and iterative reconstruction with handcrafted priors [9], [10] struggle under severe angular truncation, often failing to recover fine anatomical structures or suppress artifacts [11], [12]. Recent advances in deep learning have significantly improved LACT reconstruction by learning data-driven priors from large-scale datasets. Early convolutional neural network (CNN)-based approaches, such as FBP-ConvNet [13], demonstrated remarkable capability in restoring missing structures from undersampled projections. However, their limited receptive field and poor adaptability across different scan protocols and anatomies hinder broader application. In contrast, Transformer architectures have addressed these issues by capturing long-range contextual features through global attention mechanisms instead of localized convolutions. Recent studies [12], [14], [15] have explored attention-based architectures to improve CT reconstruction under extreme noise or data sparsity, yet most existing models rely solely on image-based supervision, ignoring valuable clinical metadata. The disconnect between imaging data and associated metadata suggests an untapped potential for metadata-aware reconstruction frameworks to enhance image fidelity.

With the increasing availability of multimodal datasets, which incorporate not only medical images but also textual data, there is a growing consensus that image reconstruction should not be treated as a purely image-domain task. In particular, Transformer-based models naturally support such integration of image and non-image information via cross-attention. Several recent studies [16], [17] have attempted to incorporate this semantic guidance, highlighting the emerging synergy between large language models (LLMs) and medical imaging tasks.

Although these works represent a promising step toward text-conditioned reconstruction, their focus on scan proto-

The paper was submitted on XXXX. This work was supported in part by NIH/NIBIB under grants R01EB032807 and R01EB034737, and NIH/NCI under grant R21CA264772. Corresponding author: H. Yu, Email: hengyong-yu@ieee.org.

The authors are with the Department of Electrical and Computer Engineering, University of Massachusetts Lowell, Lowell, MA, 01854, USA.

col prompts overlooks richer clinical metadata, limiting the breadth of semantic context for guidance. In clinical settings, metadata are inherently diverse [18], including acquisition parameters, patient demographics, and diagnostic impressions. These heterogeneous sources provide complementary information that can jointly constrain the reconstruction solution space. A unified framework that integrates diverse metadata may therefore improve both anatomical fidelity and semantic alignment in ill-posed scenarios such as LACT. To operationalize such unified conditioning, recent studies have explored the integration of Transformer into diffusion models, opening new frontiers in generative medical imaging [19], [20]. As a class of probabilistic generators, diffusion models excel at modeling the underlying distribution of high-dimensional medical data, enabling the learning of expressive priors that combine stochastic sampling with semantic constraints. Although it is still nascent to combine diffusion models with LLM-based transformers for inverse imaging problems, preliminary results suggest superior image quality in incomplete data scenarios. For example, ContextMRI [21], a metadata-conditioned diffusion model for compressed sensing MRI, incorporates detailed clinical contexts, such as anatomical region, imaging contrast, acquisition parameters, and pathology descriptions, via CLIP-based text embeddings. By using learned diffusion priors, ContextMRI significantly outperforms unconditional models, especially under extreme undersampling, at a potential cost of reduced generalizability. In the field of CT image synthesis, GenerateCT [22] employs a vision-language transformer to synthesize low-resolution CT images from text, refined by a diffusion model. These approaches collectively demonstrate a compelling solution to the longstanding challenge of ill-posed image reconstruction by integrating diffusion priors with multimodal clinical contexts.

Despite the growing success of generative modeling in medical imaging, it remains substantially more challenging for the task of LACT reconstruction than conventional image generation or super-resolution. First, medical reconstruction demands strict anatomical fidelity, leaving no tolerance for artificial lesions or structural hallucinations. This puts stringent constraints on the generative process. Second, the image degradation caused by limited-angle scanning settings poses an unfavorable condition for diffusion models, making the denoising trajectory more difficult to converge. Furthermore, LLM-guided approaches remain underexplored in LACT reconstruction, especially with guidance from structured clinical metadata. To address these challenges, we propose a metadata-guided two-stage diffusion framework for cardiac LACT reconstruction, as shown in Fig.1. Overall, this model employs clinical text to progressively generate high-resolution CT images and employs incomplete sinograms to ensure the consistency of the generated images with the actual object, thereby obtaining high-fidelity CT images suitable for clinic.

Main contributions of this work are summarized as follows:

- **Metadata-guided two-stage framework:** A cascaded diffusion pipeline is proposed for LACT reconstruction. The first stage synthesizes coarse priors from clinical metadata, while the second restores fine details conditioned on both coarse image and metadata embeddings.

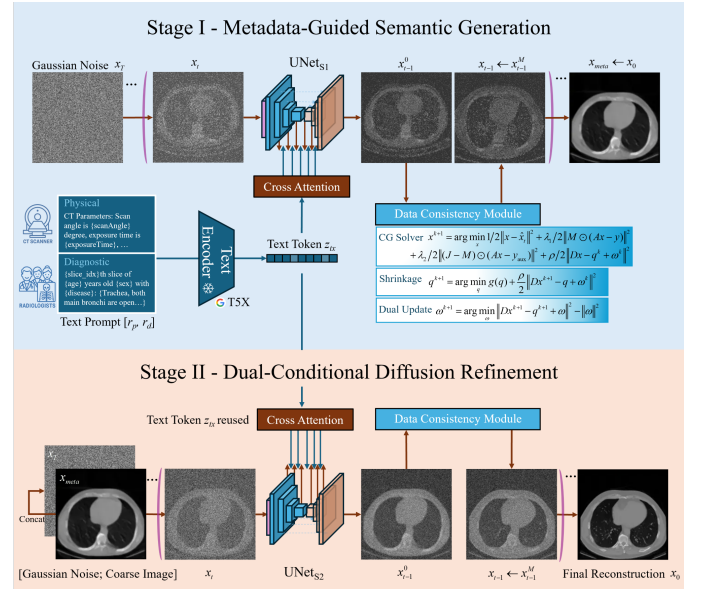


**Fig. 1:** Two-stage framework for LACT reconstruction via text-guided diffusion and projection-domain consistency. Stage I employs a vision-language transformer conditioned on metadata to generate a semantically consistent coarse image. Stage II refines the image guided by both the coarse image and text token. At each denoising timestep, a data consistency module, including CG solver, shrinkage operator, and dual variable updates, integrates projection-domain constraints.

- **Structured semantic conditioning from different metadata:** The framework integrates multiple forms of structured metadata, including acquisition parameters, patient demographics, and diagnostic impressions, into two generative stages. This design enables semantic guidance in the absence of image inputs in the early phase, promoting generalizability across different acquisition scenarios.
- **Physics-informed generative modeling:** An ADMM-based data consistency module is integrated at each sampling step in two stages to enforce fidelity to the measured sinogram. This ensures alignment between semantic priors and measurements, resulting in improved anatomical accuracy under severe angular truncation.
- **Comprehensive evaluation:** Extensive experiments on simulated and real cardiac LACT datasets demonstrate the superiority of the proposed method over state-of-the-art (SOTA) iterative and learning-based baselines, particularly in restoring details under severe angular truncation.

## II. METHODOLOGY

### A. Problem Formulation and Framework Overview

The CT imaging process can be modeled as a discrete linear system:

$$y = Ax + b, \quad (1)$$

where  $x \in \mathbb{R}^{HW}$  denotes the vectorized object to be reconstructed,  $H$  and  $W$  represent the height and width of the object,  $A \in \mathbb{R}^{P \times HW}$  is a system matrix to represent the forward projection operator,  $y \in \mathbb{R}^P$  is the measured

vectorized sinogram of  $x$  via the CT scanner, and  $b$  represents measurement noise. In LACT, only a subset of angular views is available. The imaging model is then reformulated as (2):

$$y = M \odot (Ax + b), \quad (2)$$

where  $M \in \{0, 1\}^P$  is a binary angular truncation mask to indicate the angular positions of sampled views, and  $\odot$  denotes element-wise multiplication. This truncation yields incomplete projection, creating a severely ill-posed inverse problem where conventional analytical methods fail to recover fine structures.

To address this LACT problem, we propose a generative reconstruction framework that integrates semantic priors derived from structured clinical metadata with projection-domain constraints. This design enables high-fidelity reconstructions under severely undersampled conditions by jointly leveraging both semantic and measurement-driven guidance. As shown in Fig.1, the pipeline consists of two cascaded stages:

The first stage uses a diffusion model conditioned exclusively on clinical metadata to reconstruct a coarse anatomical image from pure noise. This metadata includes structured scan parameters (e.g., exposure time, scan angle), demographics (e.g., age, sex) and radiological impressions, encoded with a pretrained T5X encoder [23], [24]. The model employs a transformer-based UNet with cross-attention to inject semantic context into the denoising process. Sampling follows the Elucidated Diffusion Model (EDM) formulation. The second stage further refines the coarse output conditioned on both the coarse image from Stage I and the clinical metadata. Operating at higher spatial resolution, this stage focuses on recovering subtle details and improving local consistency. This process is also governed by EDM-style sampling. Each timestep for both sampling processes is followed by an ADMM-based consistency module to minimize a composite loss that balances proximity to the model prediction, fidelity to the measurement, and regularization on image gradients. This architecture enables semantically meaningful reconstructions while ensuring physical plausibility across the generative trajectory.

## B. Data Curation

The training dataset is derived from the CTRATE dataset [25], a public collection of chest CT volumes with paired acquisition parameters, demographics, and diagnostic reports, making it well-suited for multimodal learning. From the CTRATE training split, we randomly select 1,000 patient cases to construct our training dataset. To reduce computational cost and memory usage during model training, each 3D volume is decomposed into multiple 2D axial slices for LACT reconstruction. Since each slice should retain clinically relevant information, we associate metadata from 3D report to 2D domain as follows: each group of 20 contiguous axial slices is first processed by CTCLIP [25], a pretrained clinical-language model for CTRATE, to predict group-level diagnostic labels. These labels, along with the original radiology reports, are then assigned to all slices within the group. Additional metadata, including patient age, sex, and slice position within the 3D volume, are also assigned to each slice.

Inspired by recent success in metadata-guided image reconstruction for MRI [21] and CT [16], which demonstrate

the importance of acquisition parameters in learning-based recovery from sparse measurements, we incorporate acquisition parameters as part of metadata. In total, the training dataset comprises 46,250 full-angle 2D CT images. Each image is forward-projected using CTCLIP [26] to generate fan-beam sinograms, which are subsequently angularly truncated under six acquisition ranges: 60°, 90°, 120°, 150°, 180°, and 360°. This procedure yields 277,500 2D instances, each consisting of an original image, a corresponding sinogram, and structured metadata. Each image includes 512×512 pixels, and the full-view sinograms have 900 detector bins and 1,000 angles.

For testing, we randomly sample 200 patients from the CTRATE testing split, yielding a total of 55,500 2D CT image-sinogram-metadata pairs after the same preprocessing pipeline. Besides, we evaluate generalization and effectiveness on a clinical cardiac dataset acquired with a GE Discovery CT750 HD scanner, approved by the Institutional Review Boards of the Vanderbilt University Medical Center and the University of Massachusetts Lowell. A total of 12 patient rawdata are acquired over a full angular range of 360°, yielding 984 views per case, with each projection consisting of 835 detector elements. The distance from the X-ray source to the rotation center and to the detector are 625.6 mm and 1097.0 mm, respectively. The original projections are subsequently truncated to simulate the limited-angle scans at 90° and 120°.

To standardize the input across all models, the available metadata (acquisition parameters, demographics and diagnostic reports) are formatted into structured natural language prompts and aligned with the clinical reporting conventions used in CTCLIP, as summarized in Table I.

TABLE I: Example of Metadata Input

Type	Input Content
Physics	CT Parameters: Scan angle is {scanAngle} degree, exposure time is {exposureTime}, X-Ray tube current is {tubeCurrent}.
Demography & Diagnosis	{slice_idx}th slice of {age} years old {sex} with {diseases}: {Trachea open, left lung partially collapsed, large pleural effusion...}.

## C. Metadata-guided Diffusion for LACT Generation

1) *Metadata-conditioned Diffusion Sampling*: The first stage of our framework employs a weakly conditional diffusion model to generate a coarse CT image directly from clinical metadata. Unlike supervised methods that rely on corrupted reconstructions (e.g. FBP images) as inputs conditions, this model synthesizes the anatomical structures entirely from noise, guided by semantic priors encoded in textual metadata. Each slice is paired with a structured text prompt  $r = [r_p; r_{de}; r_{di}]$ , where  $r_p$  contains physical acquisition parameters,  $r_{de}$  includes patient demographic information, and  $r_{di}$  represents diagnostic metadata generated by aligning the full-volume radiology report with the 2D slice context. These textual inputs are embedded into a token sequence  $z_{tx} \in \mathbb{R}^{N_t \times d}$  using a pretrained language encoder T5X, where  $N_t$  is the number of text tokens and  $d$  is the embedding dimension.

The image generation process begins from a random noise image  $x_T \sim N(0, I)$ . A model parameterized via  $\theta$  iteratively



denoises the image across a sequence of diffusion steps  $t = T \rightarrow 0$ , following the velocity-based EDM formulation:

$$\begin{aligned} x_{t-1} &= x_t + \Delta t \cdot d_i + \sqrt{\omega_t(t_i)\Delta t} \cdot \epsilon_i, \text{ with} \\ d_i &= v_\theta(x_t, t_i, z_{\text{tx}}) + \frac{1}{2}\omega(t_i) \cdot s_\theta(x_t, t_i, z_{\text{tx}}), \end{aligned} \quad (3)$$

where  $v_\theta$  denotes the predicted velocity field,  $s_\theta$  is the approximated score function, representing the log-density gradient at time  $t$ ,  $\omega(t)$  denotes a time-dependent noise scale and  $\epsilon \sim N(0, I)$  is the Gaussian noise. The final output of Stage I at  $t = 0$  ( $x_{\text{meta}}$ ), corrected by data consistency in Sec.II-C.3 serves as a coarse anatomical condition for Stage II.

While the first stage focuses on recovering global semantic structures from clinical metadata, the second stage model aims to restore high-frequency details and suppress residual artifacts. This process is conditioned on both image-level features from coarse  $x_{\text{meta}}$  and the metadata embedding  $z_{\text{tx}}$ , forming a dual-constraint mechanism. At each sampling timestep  $t$ , the model receives the noisy image  $x_t$  and produces an intermediate estimate via the update:

$$\begin{aligned} x_{t-1}^* &= x_t^* + \Delta t \cdot d_i^* + \sqrt{\omega_t(t_i)\Delta t} \cdot \epsilon_i, \text{ with} \\ d_i^* &= v_\theta(x_t^*, t_i, \hat{x}_{\text{meta}}, z_{\text{tx}}) + \frac{1}{2}\omega(t_i) \cdot s_\theta(x_t^*, t_i, \hat{x}_{\text{meta}}, z_{\text{tx}}). \end{aligned} \quad (4)$$

**2) Model Architecture:** To incorporate metadata prior, the architecture for both stages adopts a transformer-based UNet with cross-attention mechanisms. The noisy image input, either  $x_t$  in Stage I or the cascaded pair  $[x_t^*; \hat{x}_{\text{meta}}]$  in Stage II, is first mapped into spatial tokens  $z_{\text{im}} \in \mathbb{R}^{N_v \times d}$  via a multi-scale patch embedding module. The intermediate feature  $z_{\text{im}}^l$ , metadata token  $z_{\text{tx}}$ , and time embedding  $h_{\text{time}}$  are jointly fed into the core encoder/decoder blocks.

As detailed in Fig.2, each encoder/decoder block of the network contains three submodules: **Cross-Attention (CA)** allows image feature  $z_{\text{im}}^l$ , processed via a convolutional block (ConvBlock), to attend to relevant metadata embeddings  $z_{\text{tx}}$ :

$$q_n = W_q z_{\text{tx}(n)}, k_n = W_k z_{\text{tx}(n)}, v_n = W_v z_{\text{im}(n)}, \quad (5)$$

$$z_n' = \text{softmax}\left(\frac{q_n^T k_n}{\sqrt{d}}\right) v_n, \quad (6)$$

where  $W_q$ ,  $W_k$ , and  $W_v \in \mathbb{R}^{d \times d_h}$  are learnable projection matrices, thereby infusing domain-specific semantic priors into the generation process. **Time Embedding (TE)** encodes the continuous noise scale using log-SNR, which is first embedded via sinusoidal positional encoding, and then projected by a multilayer perceptron (MLP) into FiLM-style scale and shift parameters. These parameters modulate GroupNorm-normalized feature maps via an affine transformation, enabling time-aware adaptation of the feature stream. The modulated features are subsequently passed through an activation function and a convolution layer, providing noise-level-dependent conditioning, aligned with the conditioning paradigm in EDM. **Guided Contextual Attention (GCA)** is a spatial feature matching mechanism to employ channel attention to further enhance structural coherence. As shown in Fig.2, GCA is

inserted after the CA module and TE modulation. The updated feature is computed as:

$$\begin{cases} z_{\text{im}}' = \text{ConvBlock}(z_{\text{im}}^l) \\ z_{\text{comb}}^l = z_{\text{im}}' + \text{CA}(z_{\text{im}}', \text{Concat}(z_{\text{tx}}, h_{\text{time}})) \\ z_{\text{im}}^{l+1} = z_{\text{im}}^l + \text{Conv}(\text{GCA}(\text{TE}(h_{\text{time}}, z_{\text{comb}}^l))), \end{cases} \quad (7)$$

and the output is propagated to the next UNet layer as  $z_{\text{im}}^{l+1}$ .

**3) Data Consistency Regularization:** Although the metadata-conditioned diffusion model provides strong semantic priors, the generated image at each timestep may still deviate from the actual image due to the absence of directly measured sinogram, as shown in Fig.3. To bridge this gap, we integrate a physics-based consistency module using ADMM. After each denoising step, the predicted image  $\hat{x}_{t-1}$  is refined by solving:

$$\begin{aligned} x_{t-1} &= \arg \min_x \frac{1}{2} \|x - \hat{x}_{t-1}\|^2 + \frac{\lambda_1}{2} \|M \odot (Ax - y)\|^2 \\ &\quad + \frac{\lambda_2}{2} \|(J - M) \odot (Ax - y_{\text{aux}})\|^2 + \mu R(Dx), \end{aligned} \quad (8)$$

where  $y$  is the measured LACT sinogram,  $y_{\text{aux}}$  represents an auxiliary sinogram guidance (e.g., derived from Symmetric-Geometry or interpolation),  $J$  is an all-ones matrix,  $R$  is a regularization term, specifically expressed as isotropic TV, and  $\lambda_1, \lambda_2$  and  $\mu$  are hyperparameters to balance data fidelity and regularization. Considering the unreliability of auxiliary sinogram in fine-scale reconstruction,  $\lambda_2$  exhibit an exponential decline with respect to the sampling step.

To solve this problem efficiently, we introduce an auxiliary variable  $q = Dx$  and recast the regularization as a separable constraint. The corresponding augmented Lagrangian is:

$$L_p(x, q, \omega) = f(x) + g(q) + \frac{\rho}{2} \|Dx - q + \omega\|^2 - \frac{\rho}{2} \|\omega\|^2, \quad (9)$$

where  $\omega$  is the dual variable,  $f(x)$  contains all the  $x$ -related terms, and  $g(q)$  denotes TV regularization. The iterative ADMM is applied to solve Eq.(9). In practice, the  $x$ - and  $q$ -subproblems are solved by conjugate gradient (CG) method [27] and soft-thresholding method, respectively, while  $\omega$  is updated in a closed form. This correction ensures the denoised image at each diffusion sampling step remains both semantically plausible and physically consistent.

For network training, Stage I is trained to reconstruct a low-resolution and Pseudo-full-view CT image from noise of different levels via weakly supervised learning on clinical metadata. Quadruple down-sampled images serve as references to mitigate the difficulty of the image generation task and improve training stability. For Stage II, an identical network architecture is employed to refine the coarse image generated by Stage I after being corrected by ADMM-based data consistency module. The input to this stage is the concatenation of Gaussian noise and a four-fold upsampled version of the physically consistent coarse image. The full-view image reconstructed by FBP is used as a training reference in this stage. Both Stage I and Stage II models are trained using pixel-wise  $L_2$  loss between the predicted output and the corresponding reference.



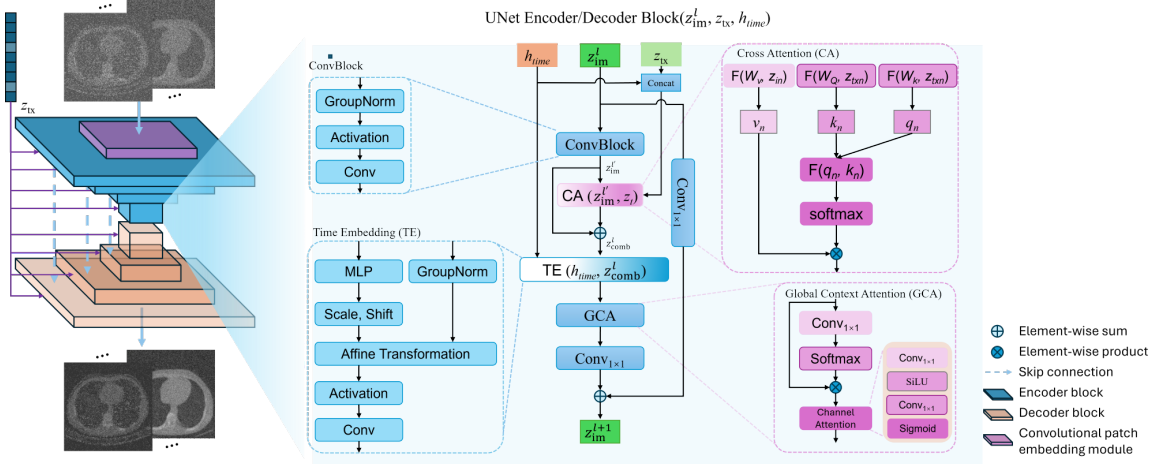


Fig. 2: Internal architecture of the conditional UNet Encoder/Decoder Block in the proposed diffusion framework.

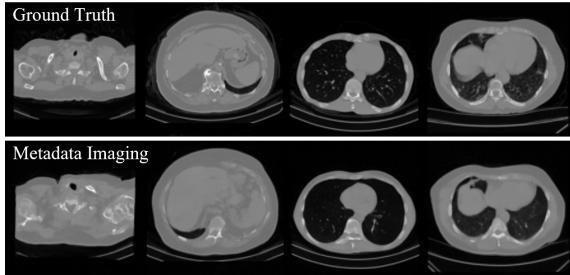


Fig. 3: Visual comparison of metadata-conditioned image generation with ground-truth chest CT cases. Each column pair shows the synthesized image from the metadata-guided diffusion model (bottom) and the full-view reference (top).

### III. EXPERIMENTS SETUP

We evaluate our proposed method on both simulated and real cardiac CT datasets under various limited-angle configurations. The data preparation process, including acquisition, preprocessing, metadata extraction, and forward projection simulation, has been detailed in Section II-B. We briefly summarize the experimental setup below, including baseline comparisons, implementation details, and evaluation metrics.

**1) Competing Methods:** To evaluate the effectiveness of our proposed framework, we compare it against a comprehensive set of traditional and learning-based baselines, including FBP, ADMM-TV [28], FBPCNet [29], and recent diffusion models. DOLCE [30] is a SOTA conditional diffusion model for limited-angle CT, which incorporates sinogram and image conditions into a score-based generative model with learnable priors and projection consistency. We reproduce DOLCE with the official code and adapt it to our dataset and angular settings for fair comparison. In contrast, Decomposed Diffusion Sampler (DDS) [27] is a recent unconditional diffusion model to accelerate large-scale inverse problems. It separates the sampling process from data consistency to flexibly incorporate forward models. We compare against DDS to assess the benefit of conditioning on metadata priors. All competing methods are retrained or adapted using the same CTRATE training and testing splits, and evaluated under consistent angular truncation

masks. For fairness, model-based and learning-based methods receive the same measured sinogram and forward operator (CTLIB) during evaluation.

**2) Implementation Details:** All experiments are implemented in PyTorch 2.6.0 and conducted on Jetstream2 at Indiana University with a single NVIDIA A100 GPU (40 GB) from the Advanced Cyberinfrastructure Coordination Ecosystem: Services & Support program. For the cascaded diffusion model, each Transformer-based UNet is trained for 20 epochs, reaching 950,000 iterations with a batch size of 4. Both networks are optimized with Adam optimizer with an initial learning rate of  $1.0 \times 10^{-4}$ . Networks are trained with targets of size  $128 \times 128$  and  $512 \times 512$  for low and high resolution. In the data consistency module, we set  $K = 2$  for Stage I to rapidly solve subproblems. The corresponding regularization parameters  $\lambda_1$ ,  $\lambda_2$  and  $\rho$  are empirically selected as 4.0, 20.0 and 1.0, respectively. For Stage II,  $K$ ,  $\lambda_1$ ,  $\lambda_2$ , and  $\rho$  are set to 6, 2.0, 0.0, and 0.2, respectively.

**3) Evaluation Metrics:** We evaluate image quality using five common metrics, including peak signal-to-noise ratio (PSNR), structural similarity index (SSIM), normalized root-mean-square-error (nRMSE), Pearson correlation coefficient (PCC), and normalized mutual information (nMI) [31]. nMI quantifies the shared information content between the reconstructed image and the reference. In our implementation, nMI is computed with scikit-image, ranging from 1 to 2, with higher values reflecting greater similarity in intensity distributions and structural patterns between the reconstruction and the reference. All metrics are averaged across testing slices.

## IV. RESULTS

### A. CTRATE Dataset

Fig. 4 presents qualitative comparisons of reconstructions via different methods across  $120^\circ$ ,  $90^\circ$ , and  $60^\circ$  LACT setting. Each column depicts reconstructions via different methods, with magnified patches highlighting anatomical differences.

For  $120^\circ$  data acquisition, all deep learning methods are capable of recovering fine structures. Supervised learning methods such as FBPCNet and DOLCE exhibit local

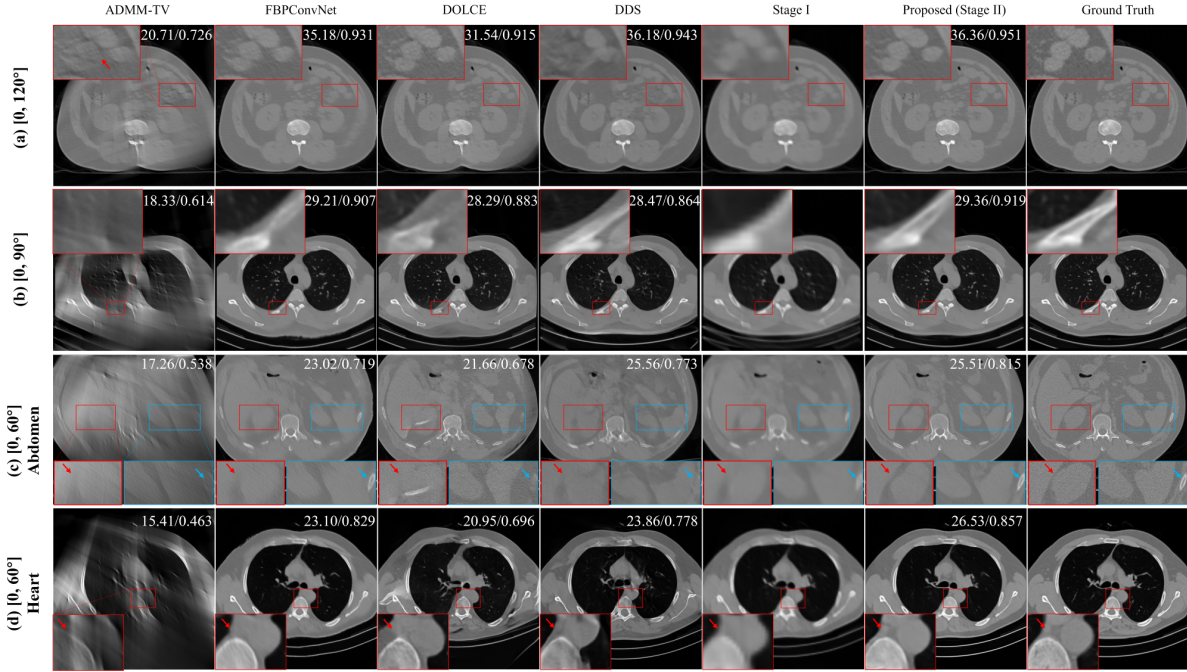


Fig. 4: Comparison of the SOTA methods for fan-beam LACT at 120°, 90° and 60° with  $[-1000, 1000]$  HU display window.

details close to the reference, especially in multiple rounded soft-tissues marked by red boxes in Fig.4 (a). Although the unsupervised DDS model yields sharper edges and bone contrast, it introduces artifacts in soft tissue areas, which potentially affect diagnosis. Our method achieves soft-tissue recovery comparable to DOLCE, and artifact suppression better than other methods, suggesting benefits of metadata guidance in integrating data fidelity of supervised learning with global distribution modeling of unsupervised approaches.

As the angle narrows, the advantage of semantic guidance becomes more pronounced. In a case of bone structure recovery at 90°, only the proposed method reconstructs bone patterns visibly consistent with the ground truth (Fig.4 (b)). When the angle further decreases to 60°, the recovery of low-contrast soft tissues becomes significantly more challenging. As shown in Fig.4 (c), FBPCConvNet produces blurry soft tissue regions with severely diminished contrast. Diffusion-based methods partially alleviate this issue, but still lose structural consistencies. Our method produces the most faithful reconstructions, with minimal artifacts and well-preserved details. Similar trends are observed in cardiac images in Fig.4 (d).

Table. II summarizes quantitative results on the CTRATE testing set. As expected, learning-based approaches outperform analytical and iterative baselines. FBPCConvNet yields high nMI and PCC from its ability to capture global contrast and coarse structure with large training data. However, as the angular range decreases, its performance on SSIM, PSNR, and RMSE metrics lags behind DDS, revealing limited capacity for texture preservation under LACT conditions. DDS shows stronger capability to reconstruct high-frequency details, consistent with Fig. 4. DOLCE remains competitive at moderate truncation but exhibits instability across the CTRATE testing set, due to the difficulty of tuning hyperparameters across diverse cases. As a result, its average performance

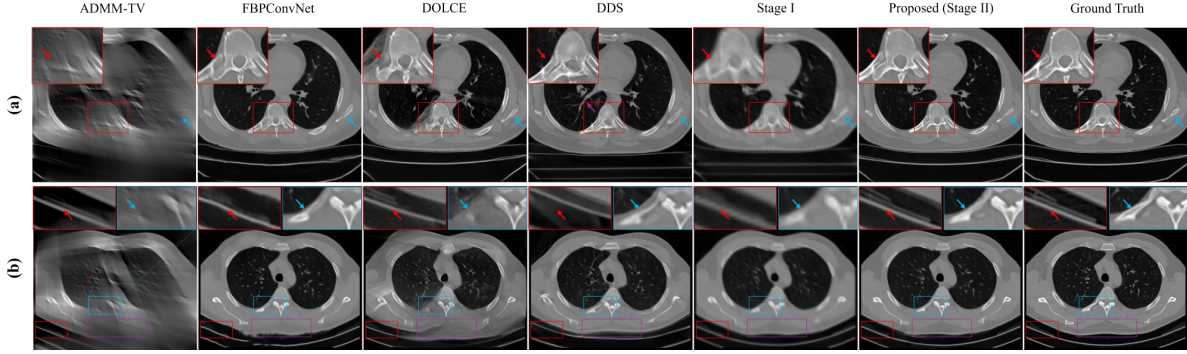
falls behind that of DDS and FBPCConvNet. In contrast, our method consistently ranks first or second across all metrics and angular settings. Compared to DDS (runner-up), it improves SSIM/PSNR by 3.02%/2.93% at 90° and 3.49%/4.36% at 60°, showing the added value of metadata integration via a two-stage transformer-based UNet for LACT imaging.

To evaluate the generalizability of the proposed method, we conduct two out-of-distribution experiments on CTRATE: one using fan-beam CT projection at a 75° angular range, which was not included in the training set, and the other with 45° parallel-beam projections, whose angle and geometry do not appear during training. Results of the first experiment are presented in Fig.5. In high-contrast bony regions (Fig.5 (a)), FBPCConvNet reconstructs the gross structure of the thoracic vertebrae, but fails to resolve the interspaces between the vertebrae and ribs (red arrows), and degrades in severely truncated areas (blue arrow). Due to domain shift between the training and testing distributions, DOLCE introduces ground-glass-like artifacts above the ribs, which may lead to misdiagnosis. DDS improves edge sharpness and bone contrast but generates artificial textures, as highlighted by purple arrow in Fig.5 (a). Our method provides sharp vertebral reconstructions and clear separation between vertebrae and ribs with minimal hallucinations. In soft-tissue evaluation (Fig.5 (b)), both FBPCConvNet and DOLCE fail to recover clean anatomical contours, while DDS offers sharper edges that still deviate from the reference. The proposed method achieves the most faithful visual appearance, especially in missing-data regions, where it reconstructs realistic structure and soft-tissue contrast closely aligned with the ground truth.

Quantitative results in Table III further support the visual observations. While FBPCConvNet achieves the second-best nMI and PCC, and DDS achieves the second-best SSIM, RMSE, and PSNR, our method outperforms all baselines.

**TABLE II:** Quantitative comparison of reconstruction methods on CTRATE datasets under limited-angle scenarios that have appeared in the training process.

Method	120°					90°					60°				
	SSIM	RMSE	PSNR	nMI	PCC	SSIM	RMSE	PSNR	nMI	PCC	SSIM	RMSE	PSNR	nMI	PCC
FBP	0.489	0.222	13.130	1.110	0.853	0.384	0.259	11.767	1.063	0.662	0.311	0.291	10.764	1.042	0.398
ADMM-TV	0.751	0.070	23.329	1.169	0.950	0.605	0.108	19.409	1.120	0.881	0.515	0.506	13.999	1.089	0.778
FBPConvNet	0.921	0.023	32.852	<u>1.347</u>	<b>0.995</b>	0.803	0.053	25.566	<u>1.244</u>	<u>0.972</u>	0.783	0.080	22.462	<u>1.218</u>	<u>0.918</u>
DOLCE	0.915	0.023	32.762	1.251	<u>0.984</u>	0.808	0.050	26.364	1.204	0.967	0.715	0.081	22.134	1.149	0.912
DDS	<u>0.929</u>	<u>0.022</u>	<u>33.701</u>	1.297	0.981	<u>0.861</u>	<u>0.039</u>	<u>28.214</u>	1.204	0.939	<u>0.803</u>	<u>0.057</u>	<u>25.059</u>	1.145	0.872
<b>Proposed</b>	<b>0.935</b>	<b>0.021</b>	<b>33.740</b>	<b>1.355</b>	<b>0.995</b>	<b>0.887</b>	<b>0.036</b>	<b>29.042</b>	<b>1.290</b>	<b>0.987</b>	<b>0.831</b>	<b>0.053</b>	<b>26.148</b>	<b>1.241</b>	<b>0.976</b>

**Fig. 5:** Comparison of the SOTA methods for fan-beam LACT with 75° scan. The display window is  $[-1000, 1000]$  HU.**TABLE III:** Quantitative comparison on CTRATE under unseen LACT acquisition settings.

Method	SSIM	RMSE	PSNR	nMI	PCC
<b>75° (fan-beam)</b>					
FBP	0.386	0.272	11.306	1.045	0.538
ADMM-TV	0.544	0.144	16.863	1.093	0.785
FBPConvNet	0.779	0.088	21.432	<u>1.230</u>	<u>0.957</u>
DOLCE	0.778	0.063	23.640	1.198	0.946
DDS	<u>0.814</u>	<u>0.048</u>	<u>26.489</u>	1.187	0.912
<b>Proposed</b>	<b>0.864</b>	<b>0.040</b>	<b>27.983</b>	<b>1.281</b>	<b>0.983</b>
<b>45° (parallel-beam)</b>					
FBP	0.279	0.294	10.618	1.038	0.479
ADMM-TV	0.434	0.173	15.218	1.066	0.667
FBPConvNet	0.682	0.104	19.818	1.167	0.893
DOLCE	0.694	0.097	20.363	<u>1.197</u>	<u>0.896</u>
DDS	<u>0.739</u>	<u>0.079</u>	<u>22.051</u>	1.112	0.757
<b>Proposed</b>	<b>0.800</b>	<b>0.071</b>	<b>23.414</b>	<b>1.227</b>	<b>0.955</b>

Compared to the second-best, it improves SSIM, RMSE, PSNR, nMI, and PCC by 6.14%, 16.67%, 5.64%, 4.15%, and 2.72%, respectively. Overall, the results for 75° fan-beam setting are consistent with those under 90° and 60°, as this intermediate setting lies within the training distribution. Most learning-based models adapt well to this mild distribution shift.

The second experiment is more challenging, involving both an unseen angular range (45°) and a new acquisition geometry (parallel-beam). As shown in Fig.6, FBPConvNet introduces pronounced artifacts in the data-missing regions, while DOLCE reconstructs object sizes roughly but fails to suppress boundary artifacts and exhibits banding and brightness fluctuations across soft-tissue regions. DDS yields perceptually cleaner results than supervised methods but still suffers from shape distortion and inaccurate boundaries, indicating its limited capability in preserving accurate spatial geometry under substantial distribution shifts. In contrast, our

method achieves the highest visual fidelity, with structures closely matching the reference in both perceptual quality and anatomy. These observations are corroborated by the quantitative results in Table III, where our method outperforms the second-best method by 8.25%, 10.13%, 6.18%, 2.51%, and 6.58% on SSIM, RMSE, PSNR, nMI, and PCC, respectively. Furthermore, in this challenging setting, strongly supervised learning methods (e.g., FBPConvNet and DOLCE) degrade clearly under domain shift, as evidenced by low SSIM and PSNR scores. This highlights their limited generalizability to unseen projection geometries and acquisition domains. On the other hand, DDS produces visually plausible outputs but underperforms in nMI and PCC, indicating reduced structural and pixel-level consistency compared to our method.

Beyond comparisons with reconstruction methods, Figs.4, 5, and 6 include intermediate results from Stage I of our framework. Although these initial reconstructions appear relatively blurry, they already exhibit reduced limited-angle artifacts compared to FBPConvNet, demonstrating the effectiveness of metadata-driven priors in guiding early-stage reconstructions.

To further assess the generalizability, we test on real cardiac CT data from a GE scanner. Due to differences in hardware, protocols, and patient populations, the GE dataset introduces a noticeable domain shift relative to CTRATE. To preserve the signal integrity, no nonlinear post-processing is applied to the raw sinograms, further amplifying the training-testing gap.

Fig. 7 presents the clinical reconstruction results. As expected, traditional iterative methods such as ADMM-TV are relatively robust to data distribution shifts, producing results with consistent visual characteristics. In contrast, FBPConvNet suffers from substantial pixel bias, leading to visible global gray-level shifts. Consequently, its SSIM, RMSE, and PSNR degrade significantly, and even fall below ADMM-TV. Nevertheless, since FBPConvNet preserves global structural



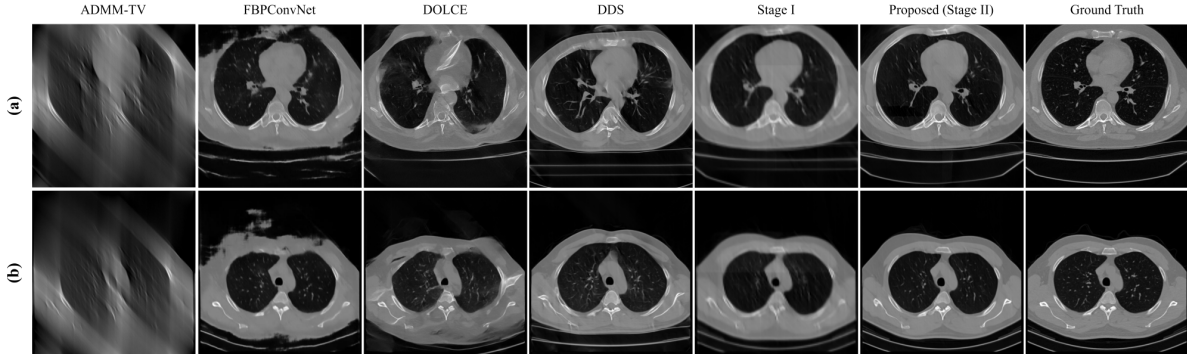


Fig. 6: Comparison of SOTA methods for parallel-beam LACT with 45° scan. The display window is  $[-1000, 1000]$  HU.

integrity to some extent, its nMI and PCC remain relatively high. DOLCE, as a supervised model, benefits from an explicit data consistency term that partially mitigates global intensity drift. However, in the 90° limited-angle setting, DOLCE fails to suppress limited-angle artifacts, unlike on CTRATE data (e.g., Fig.4(b)). DDS, which integrates unsupervised learning with data consistency, partially addresses the artifact issue in 90° scan. Building upon this, our method further leverages metadata prior during reconstruction. As a result, it consistently outperforms all baselines in structural fidelity, intensity restoration, and artifact suppression as supported by the quantitative metrics in Table IV.

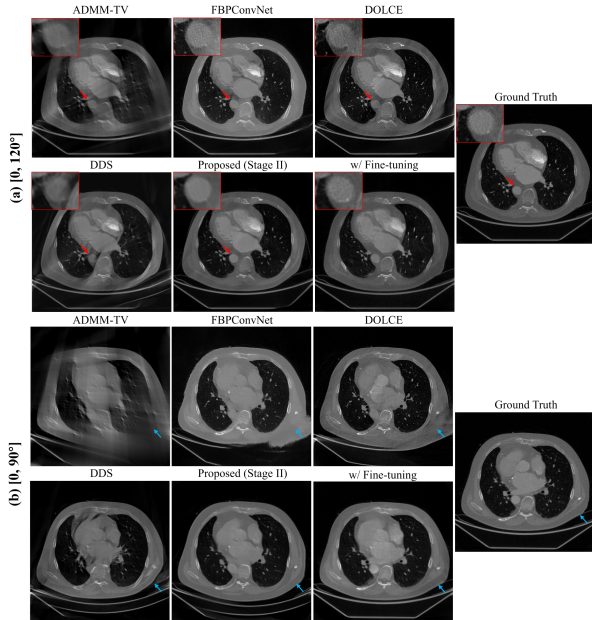


Fig. 7: Comparison of the SOTA methods for clinical data in 90° and 120° scan angles with  $[-1000, 1000]$  HU window.

### B. Ablation Study on Clinical Metadata

To evaluate the impact of different metadata priors on LACT image quality, we conduct ablation experiments on the CTRATE. Metadata are naturally categorized into three types: physical scanning parameters (tube current, exposure time, bed position and acquisition angles), demographics (patient gender and age), and diagnostic information (predicted diseases and

TABLE IV: Quantitative comparison of reconstruction methods on clinical LACT datasets.

Method	SSIM	RMSE	PSNR	nMI	PCC
<b>120°</b>					
FBP	0.417	0.172	15.304	1.090	0.853
ADMM-TV	0.710	0.073	22.747	1.118	0.904
FBPCConvNet	0.631	0.076	22.370	<u>1.168</u>	<u>0.960</u>
DOLCE	0.706	0.056	24.946	1.150	0.948
DDS	<b>0.848</b>	<u>0.033</u>	<u>29.539</u>	1.150	0.935
<b>Proposed</b>	<u>0.840</u>	<b>0.028</b>	<b>31.213</b>	<b>1.255</b>	<b>0.982</b>
<b>90°</b>					
FBP	0.329	0.195	14.230	1.058	0.718
ADMM-TV	0.643	0.089	21.055	1.094	0.854
FBPCConvNet	0.581	0.104	19.665	1.137	0.902
DOLCE	0.601	0.080	21.955	<u>1.139</u>	<u>0.907</u>
DDS	<u>0.786</u>	<u>0.046</u>	<u>26.569</u>	1.111	0.878
<b>Proposed</b>	<b>0.801</b>	<b>0.045</b>	<b>26.920</b>	<b>1.193</b>	<b>0.941</b>

physician impressions), denoted as *Phy*, *Demo*, and *Diag*, respectively. Quantitative results are summarized in Table V.

Under the 120° truncated-scan condition, where data completeness is high, metric differences among ablation variants are minimal. SSIM stabilizes at 0.935, nMI remains around 1.354, and PCC stays at 0.995, regardless of the type of metadata. The only observable change occurs in PSNR, which drops by about 0.08 dB when any single metadata type is removed. These results imply that under sufficiently complete acquisition conditions, the reconstruction model relies primarily on data consistency rather than auxiliary metadata. This finding is further supported by Fig. 4(a), where metadata-free reconstruction achieves comparable image quality with our metadata-guided reconstruction method at 120°.

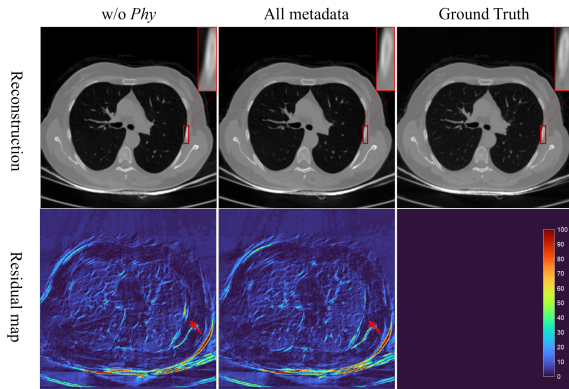
When the acquisition angle is reduced to 90°, metadata effects are more apparent. Excluding *Demo* causes the largest degradation, with SSIM, PSNR, nMI, and PCC decreasing by 0.79%, 1.07%, 0.39%, and 0.41%, respectively. Excluding *Phy* or *Diag* also reduces performance, though less, with drops of at least 0.56%, 0.60%, 0.16%, and 0.41% across the same metrics. Results at 75° follow a similar trend, reinforcing the observation that demographic metadata, although often regarded as weak or indirect, may encode nontrivial correlations that assist the reconstruction model under ill-posed conditions. One possible explanation is that in the selected 200 cases from the CTRATE testing set, certain disease categories and their associated imaging manifestations exhibit correlations with demographic factors. To explore this

**TABLE V:** Ablation study on three types of metadata. Each row corresponds to a metadata configuration.

Metadata Type			120°				90°				75°				60°			
Phy	Demo	Diag	SSIM	PSNR	nMI	PCC	SSIM	PSNR	nMI	PCC	SSIM	PSNR	nMI	PCC	SSIM	PSNR	nMI	PCC
✗	✓	✓	0.935	33.660	1.354	0.995	0.882	28.865	1.288	0.983	0.861	27.898	1.276	0.983	0.828	26.056	1.240	0.973
✓	✗	✓	0.935	33.644	1.354	0.995	0.880	28.731	1.285	0.983	0.859	27.886	1.275	0.981	0.824	26.001	1.236	0.973
✓	✓	✗	0.935	33.661	1.354	0.995	0.881	28.868	1.288	0.983	0.861	27.942	1.278	0.983	0.824	26.034	1.236	0.974
✓	✓	✓	0.935	33.740	1.355	0.995	0.887	29.042	1.290	0.987	0.864	27.983	1.281	0.983	0.831	26.148	1.241	0.976

possibility, we conduct additional statistical analyses. The five most common abnormalities are identified as lung opacity (80), lung nodule (77), lymphadenopathy (64), consolidation (55), and pulmonary fibrotic sequela (52). A Mann-Whitney U test revealed that for four of the five categories, excluding lung nodule, the p-values are  $< 0.05$ , indicating statistically significant difference in disease prevalence with respect to age.

At 60°, where projection incompleteness is most severe, all metadata types contribute positively to reconstruction quality. Removing *Demo* causes the most significant performance degradation: SSIM drops from 0.831 to 0.824, PSNR declines by 0.147 dB, and nMI decreases from 1.241 to 1.236. In this highly ill-posed setting, *Diag* and *Demo* exhibit similar effects on SSIM, nMI, and PCC, with a slight distinction in PSNR—removal of *Diag* results in a 0.114 dB drop. *Phy* shows the smallest impact on quantitative metrics. One possible explanation is that certain physical priors, such as acquisition geometry, are already partially embedded in the system matrix of the data consistency term. Nevertheless, the value of *Phy* metadata becomes evident when examining residual maps. As illustrated in Fig. 8, removing *Phy* metadata increases artifacts and noticeable structural shifts in the regions corresponding to missing angular data. Quantitatively, the mean difference intensity is reduced by 3.05% compared to the model conditioned on metadata without *Phy*, demonstrating the effectiveness of scanner-related metadata guidance. This indicates that physical metadata, such as acquisition angle, bed position, and tube current, serve as critical priors that influence image pattern formation and pixel-level intensity distribution, complementing the purely data-driven reconstruction pipeline. Overall, under severe undersampling, all metadata provide complementary priors, and missing any modality weakens reconstruction fidelity.

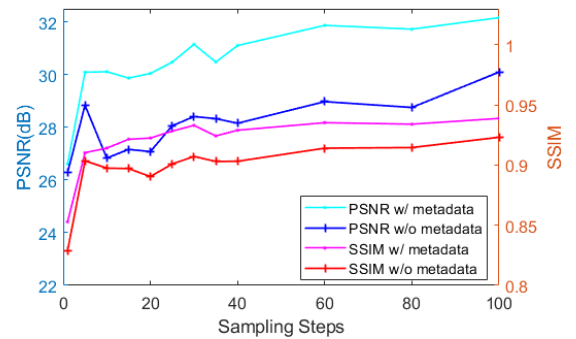
**Fig. 8:** Visual comparison of the effectiveness of *Phy* metadata in 90° scan angles. Images are normalized to  $[0, 255]$ .

## V. DISCUSSION AND CONCLUSION

This work introduces a two-stage diffusion framework that integrates structured clinical metadata to guide LACT reconstruction. Extensive experiments on both simulated and real-world datasets show significant improvement in image quality. Compared to metadata-free methods, our model achieves higher fidelity in both pixel-level accuracy and structural realism, with clearer preservation of anatomical details.

Beyond improvements in image quality, we further investigate how metadata affect the diffusion convergence. Diffusion models reconstruct images through iterative denoising steps from random noise. Metadata, when introduced, serve as structured and low-entropy priors that narrow the sampling space and guide the model toward plausible anatomical configurations. To verify this hypothesis, we conducted controlled experiments under varying sampling steps, both with and without metadata guidance. All other parameters were fixed, including the reconstruction parameters and noise initialization. This design enables a direct comparison of how metadata affect the speed and stability of the sampling process.

As shown in Fig. 9, PSNR exhibits strong oscillations in the metadata-free setting during early sampling (steps 5–10), and stabilizes only after around 30–40 steps, whereas the metadata-guided model achieves early stabilization by step 5, with only minor fluctuation near step 35. Regarding SSIM, fluctuations across sampling steps are generally smaller than for PSNR. The metadata-guided SSIM curve plateaus by step 5, while the non-guided version shows only mild variations between steps 5 and 30. Importantly, the metadata-guided model consistently outperforms its non-guided counterpart across all sampling steps. At step 40, metadata inclusion increase PSNR by 2.95 dB and SSIM by 0.026. These results suggest that metadata not only enhance final reconstruction quality but also accelerate

**Fig. 9:** Comparison of convergence behavior for models w/ and w/o metadata guidance. Experiments are conducted on the 142<sup>nd</sup> slice of patient 1 in CTRATE at 120° limited angle.

convergence by semantically constraining the solution space.

Beyond convergence behavior, we also examine cross-domain generalization. One major challenge of supervised learning models lies in their limited generalizability across domains. For instance, strongly-supervised models trained on CTRATE may produce inconsistent structures on external datasets, as shown in Fig. 7 (b). In contrast, unsupervised and weakly-supervised methods such as DDS and our proposed method show greater robustness, with fewer artifacts.

However, these models are not immune to domain shifts in non-patient regions, notably medical bed structures, which vary across scanners. A likely reason is the mismatch between the diversity of patient anatomy and the homogeneity of imaging environments in the training set. For example, CTRATE predominantly contains a double-layered supports contrary to our clinical dataset. Consequently, as observed in Fig. 7 (b), both DDS and our method tend to hallucinate a double-layered bed structure at 90° angle, despite its absence in the ground truth. To address this, we perform a lightweight domain adaptation by fine-tuning the model on two target-domain patients. After 200 iterations per stage, the adapted model successfully eliminates the bed hallucination artifact, as illustrated in Fig. 7. This result suggests that few-shot fine-tuning can effectively mitigate such distribution mismatches.

Despite the effectiveness of metadata-guided reconstruction, a key limitation lies in how diagnostic metadata are incorporated. In our framework, each slice within a 3D group is assigned the same diagnostic report, ignoring slice-specific differences. Recent work [32] shows that fine-grained processing of diagnostic text, such as extracting concise, localized and disease-relevant phrases from radiology reports, can enhance text-guided image generation. Inspired by this, future work will improve the semantic conditioning pipeline to bridge the gap between textual and spatial granularity through slice-aware report alignment and refined extraction of diagnostic reports.

In conclusion, our metadata-guided two-stage diffusion framework for LACT reconstruction achieves high image fidelity under severe truncation, while improving convergence and cross-domain robustness. The incorporation of structured clinical priors proves a simple yet powerful strategy. Future work will aim to enhance semantic alignment, reduce inference latency, and enable broader clinical deployment.

## REFERENCES

- [1] M. Lubbers *et al.*, “Comprehensive cardiac CT with myocardial perfusion imaging versus functional testing in suspected coronary artery disease: the multicenter, randomized CRESCENT-II trial,” *JACC: Cardiovascular Imaging*, vol. 11, no. 11, pp. 1625–1636, 2018.
- [2] A. Varga-Szemes, F. G. Meinel, C. N. De Cecco, S. R. Fuller, R. R. Bayer, and U. J. Schoepf, “Ct myocardial perfusion imaging,” *American Journal of Roentgenology*, vol. 204, no. 3, pp. 487–497, 2015.
- [3] J. D. Dodd and J. A. Leipsic, “Evolving developments in cardiac CT,” *Radiology*, vol. 307, no. 3, p. e222827, 2023.
- [4] W. P. Shuman *et al.*, “Prospective versus retrospective ECG gating for 64-detector CT of the coronary arteries: comparison of image quality and patient radiation dose,” *Radiology*, vol. 248, no. 2, pp. 431–437, 2008.
- [5] Y. Shi *et al.*, “Detector-trigger-based cardiac multiphase micro-CT imaging for small animals,” *Journal of X-Ray Science and Technology*, vol. 31, no. 5, pp. 1047–1066, 2023.
- [6] K. Kalisz, J. Bueche, S. S. Saboo, S. Abbara, S. Halliburton, and P. Rajiah, “Artifacts at cardiac CT: physics and solutions,” *Radiographics*, vol. 36, no. 7, pp. 2064–2083, 2016.
- [7] P. Apfaltrer *et al.*, “Enhanced temporal resolution at cardiac CT with a novel CT image reconstruction algorithm: initial patient experience,” *European Journal of Radiology*, vol. 82, no. 2, pp. 270–274, 2013.
- [8] D. Bappy, D. Kang, J. Lee, Y. Lee, and H. Baek, “Deep prior based limited-angle tomography,” in *International Conference on Pattern Recognition (ICPR)*. Springer, 2025, pp. 79–95.
- [9] Z. Zhang, B. Chen, D. Xia, E. Y. Sidky, and X. Pan, “Directional-TV algorithm for image reconstruction from limited-angular-range data,” *Medical Image Analysis*, vol. 70, p. 102030, 2021.
- [10] C. Wang, X. Wang, K. Zhao, M. Huang, X. Li, and W. Yu, “A cascading l0 regularization reconstruction method in nonsubsampling contourlet domain for limited-angle CT,” *Applied Mathematics and Computation*, vol. 451, p. 128013, 2023.
- [11] Y. Huang, O. Taubmann, X. Huang, V. Haase, G. Lauritsch, and A. Maier, “Scale-space anisotropic total variation for limited angle tomography,” *IEEE Transactions on Radiation and Plasma Medical Sciences*, vol. 2, no. 4, pp. 307–314, 2018.
- [12] Y. Xu, S. Han, D. Wang, G. Wang, J. S. Maltz, and H. Yu, “Hybrid u-net and swin-transformer network for limited-angle cardiac computed tomography,” *Physics in Medicine & Biology*, vol. 69, no. 10, p. 105012, 2024.
- [13] K. H. Jin, M. T. McCann, E. Froustey, and M. Unser, “Deep convolutional neural network for inverse problems in imaging,” *IEEE Trans. Imag. Process.*, vol. 26, no. 9, pp. 4509–4522, 2017.
- [14] J. Pan, H. Zhang, W. Wu, Z. Gao, and W. Wu, “Multi-domain integrative swin transformer network for sparse-view tomographic reconstruction,” *Patterns*, vol. 3, no. 6, 2022.
- [15] B. Morovati, S. Han, L. Zhou, D. Wang, and H. Yu, “Photon-counting CT reconstruction using separable attention-based tensor neural network prior,” in *2025 IEEE 22nd International Symposium on Biomedical Imaging (ISBI)*, 2025, pp. 1–4.
- [16] C. Ma, Z. Li, J. He, J. Zhang, Y. Zhang, and H. Shan, “Prompted contextual transformer for incomplete-view CT reconstruction,” *arXiv preprint arXiv:2312.07846*, 2023.
- [17] C. Ma *et al.*, “Radiologist-in-the-loop self-training for generalizable CT metal artifact reduction,” *IEEE Trans. Med. Imag.*, vol. 44, no. 6, pp. 2504–2514, 2025.
- [18] R. Gauriau *et al.*, “Using DICOM metadata for radiological image series categorization: a feasibility study on large clinical brain MRI datasets,” *Journal of Digital Imaging*, vol. 33, no. 3, pp. 747–762, 2020.
- [19] F. Bao *et al.*, “All are worth words: A vit backbone for diffusion models,” in *Proceedings of the IEEE/CVF Conference on Computer Vision and Pattern Recognition*, 2023, pp. 22 669–22 679.
- [20] Z. Ma *et al.*, “Efficient diffusion models: A comprehensive survey from principles to practices,” *arXiv preprint arXiv:2410.11795*, 2024.
- [21] H. Chung, D. Lee, Z. Wu, B.-H. Kim, K. L. Bouman, and J. C. Ye, “ContextMRI: Enhancing compressed sensing MRI through metadata conditioning,” *arXiv preprint arXiv:2501.04284*, 2025.
- [22] I. E. Hamamci *et al.*, “GenerateCT: Text-conditional generation of 3d chest CT volumes,” in *European Conference on Computer Vision*, 2024, pp. 126–143.
- [23] C. Raffel *et al.*, “Exploring the limits of transfer learning with a unified text-to-text transformer,” *Journal of Machine Learning Research*, vol. 21, no. 140, pp. 1–67, 2020.
- [24] A. Roberts *et al.*, “Scaling up models and data with t5x and seqio,” *arXiv preprint arXiv:2203.17189*, 2022.
- [25] I. E. Hamamci *et al.*, “Developing generalist foundation models from a multimodal dataset for 3d computed tomography,” *arXiv preprint arXiv:2403.17834*, 2024.
- [26] W. Xia *et al.*, “Magic: Manifold and graph integrative convolutional networks for low-dose CT reconstruction,” *IEEE Trans. Med. Imag.*, vol. 40, no. 12, pp. 3459–3472, 2021.
- [27] H. Chung, S. Lee, and J. C. Ye, “Decomposed diffusion sampler for accelerating large-scale inverse problems,” *arXiv preprint arXiv:2303.05754*, 2023.
- [28] R. Gao, F. Tronarp, and S. Särkkä, “Combined analysis-L1 and total variation ADMM with applications to meg brain imaging and signal reconstruction,” in *2018 26th European Signal Processing Conference (EUSIPCO)*. IEEE, 2018, pp. 1930–1934.
- [29] K. H. Jin, M. T. McCann, E. Froustey, and M. Unser, “Deep convolutional neural network for inverse problems in imaging,” *IEEE Trans. Imag. Process.*, vol. 26, no. 9, pp. 4509–4522, 2017.



- [30] J. Liu *et al.*, “Dolce: A model-based probabilistic diffusion framework for limited-angle CT reconstruction,” in *Proceedings of the IEEE/CVF International Conference on Computer Vision*, 2023, pp. 10 498–10 508.
- [31] C. Studholme, D. L. Hill, and D. J. Hawkes, “An overlap invariant entropy measure of 3D medical image alignment,” *Pattern Recognition*, vol. 32, no. 1, pp. 71–86, 1999.
- [32] X. Li *et al.*, “Text-driven tumor synthesis,” *arXiv preprint arXiv:2412.18589*, 2024.